IOPscience iopscience.iop.org

Home Search Collections Journals About Contact us My IOPscience

Isotropic etching technique for three-dimensional microball-bearing raceways

This content has been downloaded from IOPscience. Please scroll down to see the full text.

2014 J. Micromech. Microeng. 24 015021

(http://iopscience.iop.org/0960-1317/24/1/015021)

View the table of contents for this issue, or go to the journal homepage for more

Download details:

IP Address: 129.2.129.152
This content was downloaded on 17/02/2014 at 16:57

Please note that terms and conditions apply.

IOP Publishing Journal of Micromechanics and Microengineering
J. Micromech. Microeng. **24** (2014) 015021 (13pp) doi:10.1088/0960-1317/24/1/015021

Isotropic etching technique for three-dimensional microball-bearing raceways

B Hanrahan[1,2], **C M Waits**[2] **and R Ghodssi**[1]

[1] MEMS Sensors and Actuators Lab (MSAL), Department of Materials Science and Engineering, Department of Electrical and Computer Engineering, Institute for Systems Research, University of Maryland, College Park, MD 20742, USA
[2] U.S. Army Research Laboratory, Adelphi, MD 20742, USA

E-mail: ghodssi@umd.edu

Received 23 May 2013, revised 5 October 2013
Accepted for publication 22 October 2013
Published 16 December 2013

Abstract
A multi-step plasma etching technique is developed to obtain deep-grooved micro-scale ball-bearing raceways and employed in the fabrication of multiple ball-bearing supported microturbines. Deep-groove geometry has been chosen for the microball-bearing systems because of the ability to handle mixed axial and radial loads, allowing for stable, high-speed operation compared to previous iterations of the microball-bearing raceways. The multi-step inductively coupled plasma-based process is optimized to obtain $<2\%$ deviation amongst intended raceway depth, width and curvature. Etching non-uniformity is measured to be 0.15% within the raceway of a single device. The bearing dynamics with the new deep-groove geometry have been simulated. The deep-groove raceway packed with off-the-shelf precision ball-bearings provided a stability improvement over previous demonstrations of high-performance rotary micromachines operating at high speeds.

(Some figures may appear in colour only in the online journal)

Nomenclature

F_r	radial load
F_N	normal load
l'	lateral etch rate
r_b	ball radius
r_c	contact radius
r_H	housing radius
r_R	rotor radius
r_1	arbitrary parallel radius
m_b	ball mass
θ_c	contact angle
t	time
v'	vertical etch rate
x_m	mask opening width
ω_b	ball angular velocity
ω_R	rotor angular velocity

1. Introduction

Rolling bearings are an essential component of modern machinery, providing low friction and wear contact between moving parts. Specialized bearings are employed depending on their specific application, based on load, speed and geometric requirements. Rolling bearing technology has been extended to the realm of micro-electromechanical systems (MEMS) in the demonstration of high-performance linear and rotary micromachines. Proof-of-concept demonstrations of micromotors [1], microturbines [2], micropumps [3] and microgenerators [4], supported on microball-bearings have all relied non-ideal planar geometries for their bearing raceways. Ghodssi *et al* recently showed that future microfabricated bearing systems will need to accommodate for actuation-induced axial loads as well as inertia-induced radial loads, and will therefore require circular cross-sectioned bearing structures to handle the resultant load [5]. This paper describes the development of a 3D etching technique used to

  © 2014 IOP Publishing Ltd Printed in the UK

obtain uniform, circular cross-sectioned bearing raceways and their utilization in the next generation rotary microsystems, allowing for stable high-speed operation.

The geometry of the silicon micro-bearing is dictated by microfabrication techniques used to etch the bearings. Macro-bearing steel raceways are machined to near-net shape, heat treated and then lapped to achieve a mirror finish. The radius of the steel raceway is altered depending on the expected radial and axial loads, dictating contact angle of the ball to the raceway. Microfabricated bearings are machined in silicon. Silicon micromachining takes place either by dry or wet etching, isotropically or anisotropically. The anisotropic, deep reactive ion etching (DRIE) method is used to fabricate the rectangular cross-sectioned bearings used in the current microturbine device. The rectangular cross section provides a nominally flat, non-wavy surface for the balls to contact, simplifying contact mechanics calculations.

3D fabrication techniques allow a range of structures and therefore an array of applications that would otherwise be unobtainable through traditional, planar microfabrication methodologies. Successful demonstration of 3D fabrication has been performed in the lithography, deposition and etching domains. Gray-scale lithography utilizes variable transparency to obtain sloped profiles in photoresist. The sloped profiles can then be etched into the substrate material to obtain 3D structures such as micro-compressors [6] or optical fiber alignment devices [7]. The challenges of this technique include obtaining a consistent photoresist process and the significant difference in selectivity between substrate and photoresist in most etching schemes, which magnifies photoresist defects. Other 3D lithography techniques include ‘two-photon’ lithography, where a stereo light source is focused on a single spot within a photo-active material. The coincident point of the two light beams contains enough energy to alter the material, whereas each single light source does not. Up until recently the technique was extremely slow, therefore unreasonable for multi-device fabrication [8], but the speed has been increased by orders of magnitude [9]. 3D deposition techniques typically involve localized energy sources in reactive environments, such as localized electrochemical deposition [10] and focused ion beam deposition [11]. Both of these techniques are extremely slow compared to processes taking place on the wafer scale and are therefore not in common use.

Isotropic etching techniques have been employed since before widespread adoption of silicon-based transistors. The original isotropic silicon etch was based on hydrofluoric, nitric and acetic acid (HNA) chemistry, described in the seminal series by Schwartz *et al* determining the etch rates, roughness and uniformity of the HNA etch based on the composition of the acid [12]. The HNA etching chemistry is not completely independent of crystal structure which limits its use as a nearly perfect isotropic etch to a shallow etch depth before the anisotropy is realized. A wet etch process requires very careful process control of temperature and agitation, making it difficult to establish wafer-to-wafer uniformity [13].

Dry, plasma-based etching techniques are most relevant to this work. Utilization of inductively coupled plasma (ICP) etching techniques for isotropic profiles in silicon was first simulated by Marcos *et al* in [14]. Modification of the power profiles of etching and deposition steps within a DRIE process allowed for the realization of controlled cross-section thickness through the height of a column [15]. Gantz *et al* modeled and demonstrated an RIE-lag based method for 3D etching. In this work, masks were created using variable feature sizes and pitch to control the exposed area of reactants, and thus control the final etch profile [16]. The work by Larsen *et al* utilized a multi-step plasma process to create microlense molds. The authors performed a thorough study on etching parameters and the evolution of etch geometry [17]. The microlense study was a significant influence towards the development of the isotropically etched ball-bearing raceways which are the focus of this study.

Future microball-bearing utilizing systems, such as a microgenerator, will require high speeds. The top-down fabrication style of MEMS will dictate that the actuation mechanism, be it electrostatic, electromagnetic, or pneumatic will impart an axial (through wafer) load on the bearings. The centripetal force acting on the rotating balls will impart radial load scaling with velocity squared, therefore radial forces on the ball-bearing will need to be accounted for in addition to the axial load. To accomplish this, a circular raceway cross-section is imagined. A schematic of the rectangular and circular bearings can be seen in figure 1.

The microfabricated bearing raceway in figure 1(*b*) has been used in various microsystems using off-the-shelf precision ball-bearings including pumps, generators, motors and turbines, and has shown consistent operation over 200 million revolutions at 10 krpm [18] and brief operation up to 87 krpm [3]. An ultimate limiting factor in the operation of a device with the rectangular geometry is the lack of ability to accommodate significant radial load. At low speeds the friction forces between the ball and raceway are capable of restricting the ball radial motion. At high speeds, the radial forces overcome the friction forces and the ball-bearings make significant contact with the outer wall, ultimately resulting in failure. This concept is discussed theoretically in [5] and measured experimentally with on-chip accelerometers in [19]. The bearing geometry in figure 1(*c*) closely resembles the geometry used in macro-scale deep groove bearings, and has the capability to maintain contact with the ball under combined axial and radial loads. The general shape of the raceway represents the middle ground between the ideal bearing geometry and the capabilities of microfabrication. The following sections will discuss the design and fabrication of a circular cross-sectioned raceway, the ball-bearing dynamics within the circular geometry, and demonstration of the bearing utilized within a microturbine system.

The focus of this experiment is two-fold: the development of a unique isotropic etching technique to obtain the circular raceway cross-section and the design and demonstration of a microturbine supported on microball-bearings utilizing said raceway. This cross-section is realized by etching semi-circular cross sections into the surface of two mirrored wafers and then bonding them together. Obtaining semi-circular etching cross-sections required the development of

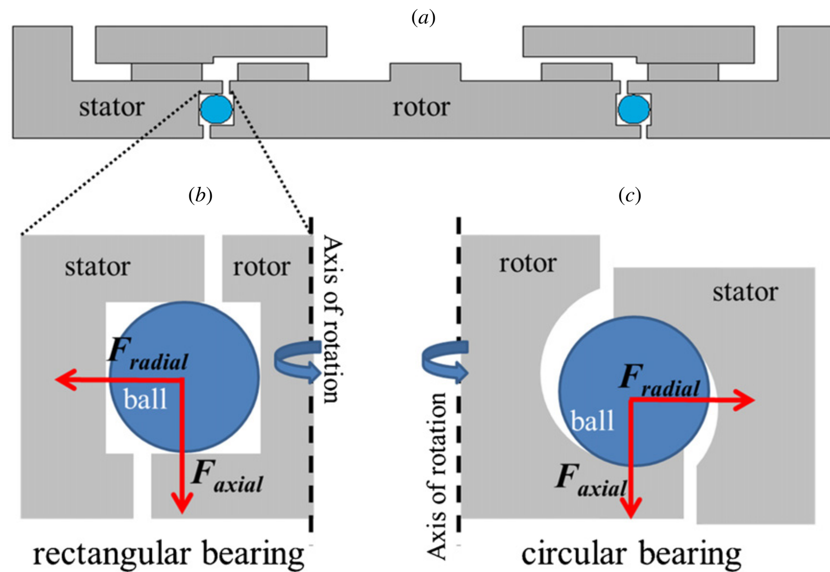

Figure 1. Comparison of bearing geometries. (*a*) Schematic of microturbine to show location of bearings. (*b*) Rectangular cross-section bearing defined by DRIE and used in previous microball-bearing devices. (*c*) Circular cross-sectioned bearing developed using custom isotropic etching techniques.

Table 1. A comparison of ball-bearing types and operating conditions.

Type:	Radial	Angular	Thrust
Macro-scale:			
Micro-scale: (imagined)			
Axial Load	Low	Medium	High
Radial Load (max. speed)	High	Medium	Low
Contact angle (est.)	0-20°	40-60°	70-90°

Deep-groove thrust bearing

a unique multi-step plasma process with tuned parameters such as power and pressure. Once the technique was demonstrated with acceptable geometries, the isotropic etching was employed within a custom fabrication flow to create the first microfabricated device with 3D bearing structures.

2. Bearing design and dynamics

Macro-scale ball-bearing systems can be categorized into three types by their desired maximum operating speed and load: thrust, angular, and radial ball-bearings. Each design is ideal for a specific ratio of axial to radial load, which is manifested in the bearing as the contact angle between the ball and the raceway. Contact angle will be discussed in detail in subsequent sections. It should also be noted that radial load capacity is analogous to maximum operating speed for these devices, as radial load is derived from centripetal forces. Table 1 compares and contrasts the three different types of ball-bearings.

Thrust bearings have a 70°–90° contact angle, resulting in an axis of rotation of the ball that is perpendicular to the axis of rotation of the rotating member. On the macro-scale this bearing is used for high-load, low-speed applications. On the micro-scale this design is often used because microfabrication techniques dictate top-down geometric alterations. As the intended speed increases, the radial load carrying capacity of the bearing system must increase as well. For systems with mixed radial and axial load, angular bearings are employed.

Table 2. Microturbine variations.

Rotor radius	Ball Material	# of balls
2.5 mm	Steel	15
	SiC	
5 mm	SiC	30

High-speed systems with dominant radial load use radial bearings where the ball axis of rotation is parallel to the rotational axis of the bearing. There are many variations of ball-bearings that fall in-between the three primary types. For this work, we fabricate deep-groove thrust bearings, which are intended for primarily axial-load situations with a higher speed tolerance than pure thrust bearings.

Multiple silicon microturbines have been designed and fabricated to serve as the proving platform for the circular cross-sectioned raceways. The variations of microturbine geometries tested in this paper are summarized in table 2. Two rotor diameters were chosen, 2.5 mm and 5 mm, both utilizing 0.5 mm balls, giving rotor:ball diameter ratios of 5:1 and 10:1, respectively. Previous microball-bearing devices had rotor:ball ratios of 35:1, whereas macro-scale bearings utilize 3–5:1 ratios, typically, to minimize the rotational inertia of the system. Stainless-steel and silicon carbide balls have been utilized because of their different densities and surface properties.

All balls tested are grade 10 or better, as defined by the American Bearing Manufacturers Association. For grade 10 rating, the lot diameter variance, ball diameter tolerance, and surface roughness must be <250 nm, <1.3 μm and <25 nm avg., respectively. To manufacture the 440C stainless-steel balls, a steel wire is first cut and pressed into the near final geometry of the ball. The ball is then progressively polished to remove flashing and eventually reach final roughness. Heat treatment of the balls is then performed to remove internal defects and reach the final hardness value. The first step in manufacturing the silicon carbide balls is a hot isostatic pressing of ceramic powder and binder, which is then sintered and ground to a final roughness and sphericity. The ratio of the hardness of the ball to the raceway should be selected such that one is not significantly harder than the other. If there is a significant hardness difference, one component will be sacrificially worn at an accelerated rate.

The microturbine presented herein, as well as any number of rotary MEMS devices utilizing ball-bearings in circular raceways can be fabricated using the scheme presented in figure 2. The microturbine is comprised of two wafers, bonded together encapsulating the ball-bearings using a technology developed by Waits *et al* in [20]. The outer surfaces of the wafers contain the turbine structures patterned in a silicon dioxide hard-mask for later use (figure 2(*a*). The inner surfaces of the wafers contain the raceways defined in figure 2(*b*) and isotropically etched in figure 2(*c*). The raceways also contain offset release structures that are defined by spray

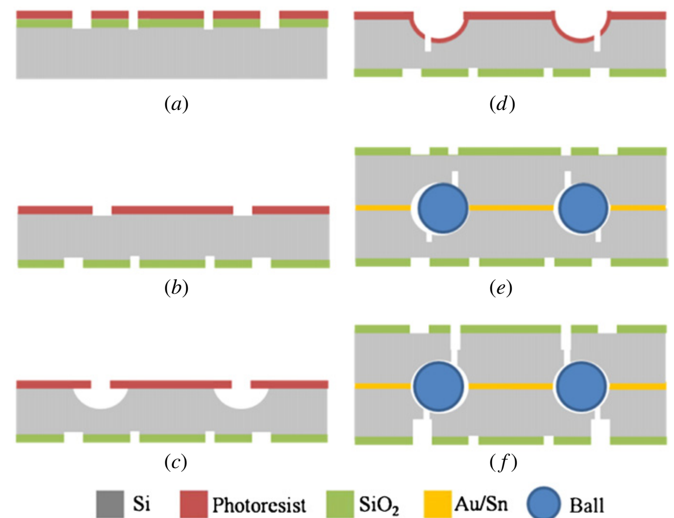

Figure 2. Fabrication scheme for rotary MEMS with circular raceways.

coat lithography and etched with DRIE to be accessed later (figure 2(*d*)). Bond alignment structures are also defined and etched during the spray-coat photoresist process on the inner surface of the two wafers. A shadow-masked evaporation of eutectic gold/tin is deposited on the inner surfaces of the wafers. Microball-bearings are then placed in the etched raceways and the two wafers are bonded (figure 2(*e*)). Finally, the silicon dioxide hard-mask patterned in figure 2(*a*) is utilized as a DRIE etch mask and the outer surfaces are etched making contact with the release etches, thereby releasing the rotor from the stator portions of the chip (figure 2(*f*)).

The most critical aspects of the fabrication are the geometry of the raceway and the location of the offset release etches. The etching techniques developed in this paper set forth the fabrication guidelines for obtaining circular raceways with rotor diameters from 1 to 10 mm. The location of the offset release etch depends on the radius of the raceway, the geometry of the rotor, the expected radial load from the desired operating speeds, and the amount of axial load tolerable. The resultant of the vector sum of radial and axial loads gives the contact angle between the ball and raceway. The offset release etch trench on the thrust (non-turbine structured) side of the rotor is radially further from the axis of rotation than center of the raceway. At increasing speeds and centripetal load the balls will push out radially towards the thrust side release etch structures. The release should therefore be offset as much as possible until the point where it is so far offset that the rotor is no longer held into position by the balls and could be completely removed from the stator. A maximum allowable contact angle of 53° was selected based upon the contact area of the ball and the desired operating parameters. This angle then determines the maximum operating speed for a given normal load. The contact angle can be calculated from equations (1) and (2):

$$\theta_c = \arctan\left(\frac{F_c}{F_N}\right) \tag{1}$$

where,

$$F_c = m_b r_R \omega_R^2. \tag{2}$$

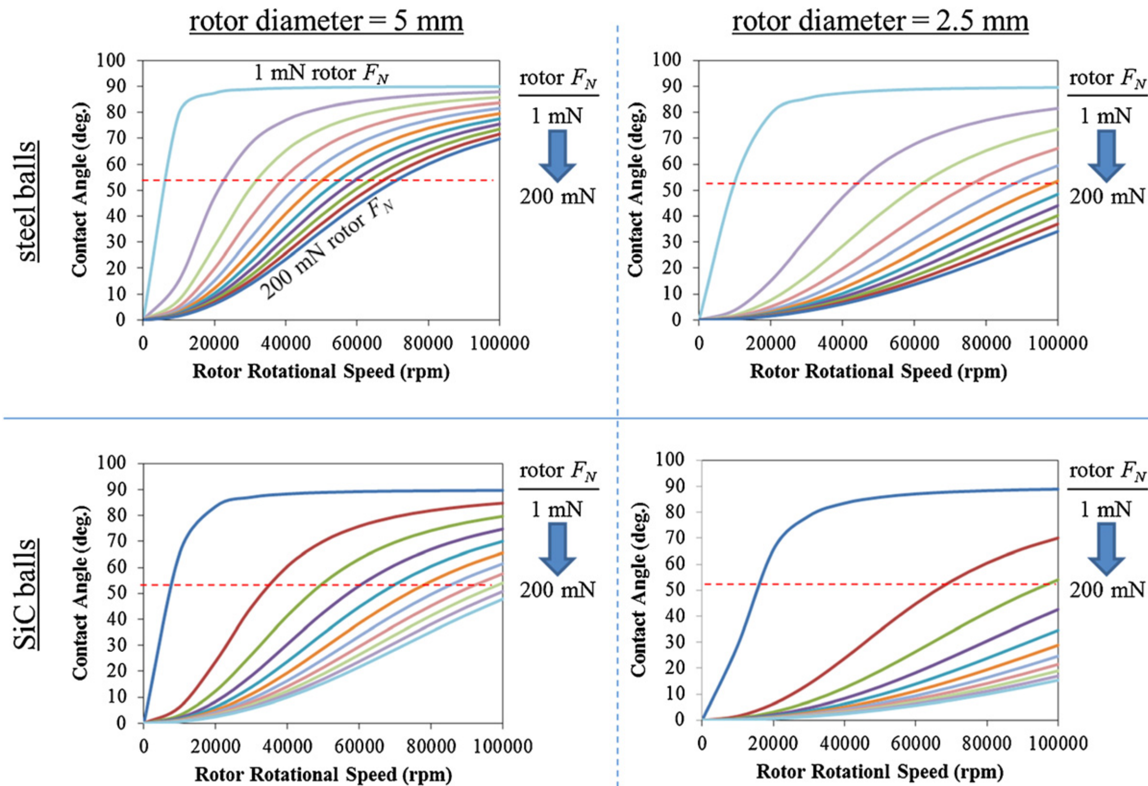

Figure 3. Numerical simulation of contact angle for tested bearing variations.

The contact angle has been simulated for a range of speeds and normal loads, based on the bearing variations outlined in table 2.

Figure 3 highlights the benefits of using smaller radii and less dense balls. In both of those cases, it requires significantly less normal load to operate at a given speed with a contact angle below the 53° geometrically defined maximum. A maximum rotor normal load of 200 mN was selected for the simulation, which equates to 250 MPa contact pressure beneath the ball. The contact pressure of the ball is calculated utilizing Hertzian contact mechanics assuming a sphere pressing on an internal cylinder, which mimics the intended geometry of the device but does not account for adhesion [21]. This contact pressure is well below the predicted 450 MPa found to result in fatigue-based raceway fracture [22].

2.1. Bearing dynamics

The geometry of the bearing presented herein could be categorized as a deep-groove thrust bearing. On the macro-scale, these bearings are used to accommodate primarily thrust (axial) loads at moderate speeds. As the contact angle increases towards the horizontal (0°) the style of bearing transitions from thrust to an angular contact to a radial bearing at or around 0°. This transition is due to the need for the axis of rotation of the ball and the principle load being nearly perpendicular in the ideal case. Of these bearing types, a radial bearing-style would be inappropriate for a microfabricated ball-bearing system because of its inability to accommodate the inevitable axial loads imparted by on-rotor actuation schemes. An angular bearing would be ideal, but this would require a press-fitting of the rotor into the stator to place a constant load on the balls and keep the rotor in place under unintended loads. This is accomplished on the macro-scale by tight machine tolerances, the utilization of thermal contractions (placing components in liquid nitrogen before assembly, for example), and minor plastic deformation allowed in the raceway. Press-fit components are not widely used in MEMS because of the brittle fracture of silicon. To obtain a microfabricated angular bearing, single micrometer tolerances would have to be obtained, balancing between being too loose to load all of the balls evenly, or so tight that the balls induce fracture of the silicon. Therefore a deep-groove thrust bearing orientation is utilized as a middle-ground between the ideal geometry and realistic fabrication capabilities, at the expense of bearing performance.

A schematic of the bearing during operation, highlighting the loads, geometries and contact angles is presented in figure 4. This figure highlights the worse-case scenario when the thrust and radial loads give a near 53° contact angle.

The contact angle, defined by the vector sum of the radial and axial load components is ideally perpendicular to the ball axis of rotation. When they are perpendicular, the center of the contact ellipse experiences pure rolling, and progressively higher magnitude sliding takes place radially outward from center. As the contact angle increases, the center of the contact ellipse moves away from the point of pure rolling, and the ball undergoes more sliding. The velocity of the sliding can be calculated from the angular velocity of the rotor and geometry, where

$$\omega_b = \frac{1}{2}\frac{r_b}{r_R}\omega_R. \tag{3}$$

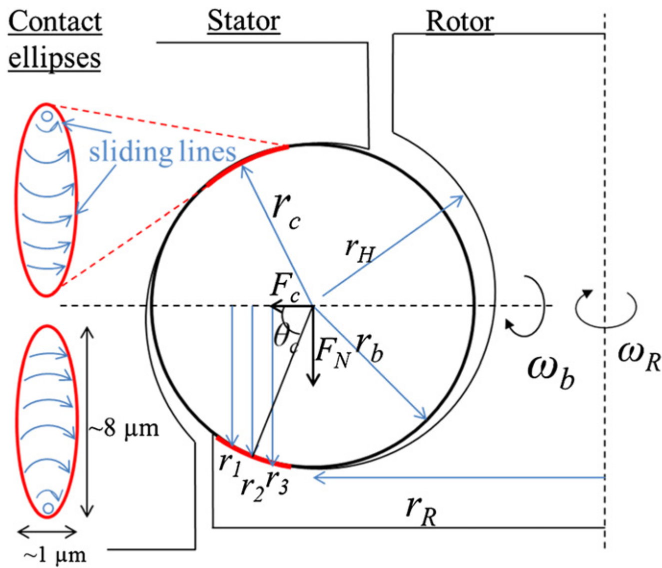

Figure 4. Bearing dynamics diagram drawn to scale for the as-fabricated raceways, showing the relationships between contact angle, force vectors and contact area. Ball contact area is approaching the offset release etch.

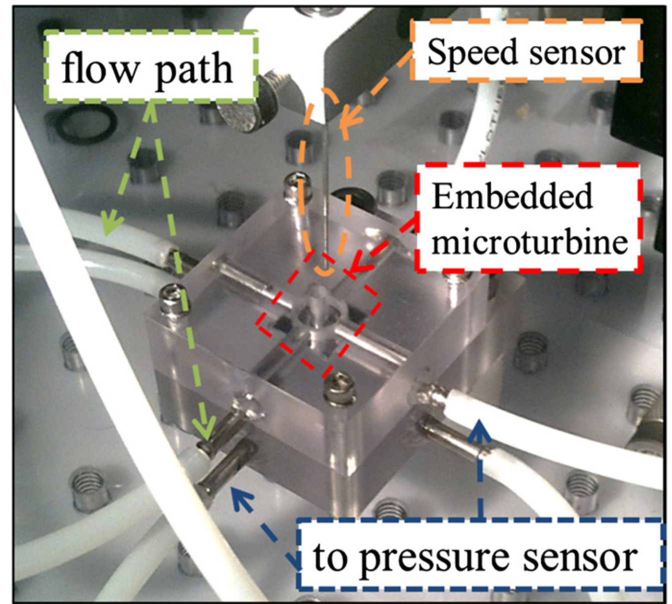

Figure 5. Photograph of packaged microturbine under test.

From the angular velocity calculated in equation (3), the linear velocity of a parallel at radius r (from figure 4) can be calculated according to the following equation:

$$V_{r_{1,2,3}} = \omega_b r_{1,2,3}. \quad (4)$$

It should be noted that there is also sliding induced from gyroscopic effects, which are not accounted for in this analysis. The gyroscopic forces on the microball bearings were found to be minimal in the rectangular bearing [22]. It is unclear the magnitude of the detrimental effect of the geometry-based sliding effects, but it is shown to be significant from the observed raceway wear, discussed in a following section.

The efficacy of the deep-groove bearing is determined by monitoring turbine performance. A custom package was designed to deliver high gas flow rates (>10 SLM) while monitoring input pressure and axial load with integrated pressure transducers and turbine speed via a tachometer-style optical displacement scheme. A picture of the packaged microturbine is provided in figure 5.

The packaging directs flow through the turbine actuation structure. During operation, some flow is allowed to leak through the backside of the device, allowing for normal load control. The package also includes ports to pressure sensors and an optical displacement sensor used to measure speed. The bearing raceways are analyzed post-mortem using scanning electron microscopy (SEM) and vertical scanning interferometry to determine the governing wear regimes.

3. Etch development

3.1. Isotropic etching development

Microfabrication technology uses an array of techniques to obtain isotropic etching profiles. These techniques include wet etching in an HNA solution or dry techniques, including XeF_2 chemical etching, or SF_6 plasma-based etching. ICP-based techniques were chosen, providing both a physical etch via ions accelerated from the plasma sputtering the substrate and a chemical component based on the well-characterized fluorination of silicon through the SF_6–silicon interaction [23, 24].

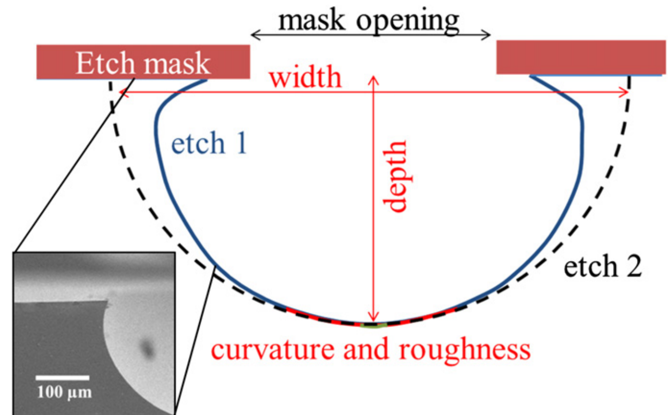

Figure 6. Graphic representation of the raceway profile during the two-step etching process. Geometric parameters of interest are highlighted. SEM image of the re-entrant profile after *etch 1* is included.

A two-step ICP process was chosen as the methodology to obtain the circular bearing cross-sections. In the two-step isotropic etch a bulk of the material is removed in the first etch and the depth and curvature are almost fully realized. The second etching step is used to remove the re-entrant silicon from beneath the masking material, ultimately widening the raceway and slightly affecting the curvature. A visual representation of the evolution of the two-step etch process is provided in figure 6. A similar process was first described by Larsen in [17] used to make batch-fabricated microlenses with good geometric control.

The important geometric characteristics of the raceway were depth, width and curvature as well as minimizing surface roughness and maximizing etch uniformity. The parameters available to tune within the ICP process were RF plate power, chamber pressure and etch time. The plate power applies a bias between the plasma and the substrate, acting on the ions from the plasma and giving the etch directionality. The chamber pressure principally affects the mean free path (MFP) of an ion in the plasma, with lower pressures providing longer paths and thus higher energy ions. Finally, it was found that the etch rates were nonlinear, so the evolution of the etch was studied with time-resolved etching.

Measurements of the etch profile were taken using optical profilometry (Veeco WKYO NT 1100). The vertical measurement resolution is 0.01 nm, while the horizontal resolution depends on the field of view, and ranged in these tests from 0.4 to 0.8 μm. The curvature of the sample was determined by fitting a circle to the average height measurement over a 50 μm wide area in the center of the bottom raceway. The roughness was measured by taking a 10 μm wide sample at the bottom of the raceway, mathematically flattening it and taking height measurements from the flattened sample. SEM of cleaved samples was utilized to confirm the profilometry measurements.

4. Results and discussion

4.1. Isotropic etching

The isotropic etch experiment took place in three distinct phases: selecting the proper etch mask geometry that results in a nearly semi-circular raceway etch, determining the exact etch parameters necessary to obtain the proper width, depth and curvature with minimal roughness, and performing a time-resolved study to determine etch rates and integrating it in the microturbine fabrication flow.

The selection of the correct masking geometry was the first challenge of the isotropic etching study. The mask's required opening (x_m) can be estimated from the vertical and lateral etch rates given by the following equations:

$$r_H = v't \tag{5}$$

$$r_H = l't + 0.5x_m \tag{6}$$

$$x_m = 2t(v' - l'). \tag{7}$$

Knowing that the ball radius is 250 μm, the raceway housing radius (r_H) can be estimated to be 260 μm at minimum. In the two-step etch process; the depth is defined in the first etching step so the time, t, can be estimated from equation (5) only. Vertical (v') and lateral (l') etch rates were assumed to be 3.6 and 2 μm min^{-1}, respectively. Substituting the time, radius and etch rates into equation (7), one obtains a mask opening of 230 μm. Because the second step in the two-step process widens the raceway w/out etching vertically (refer to figure 6), the mask opening experiments were adjusted to be centered on a 200 μm opening.

Test structures were etched using a non-optimized two-step etching process to help understand the evolution of the general shape of the raceway for different mask openings. The first isotropic etch was performed with a 10 μm *AZ9260* photoresist etch mask. The second isotropic etch was performed on the wafer after the removal of masking material. The shape ratio, defined as the ratio of etch radius (lateral distance from center of mask opening to edge of etch) to etch depth, where 1 is a semi-circle, was tracked over a range of mask openings in figure 7.

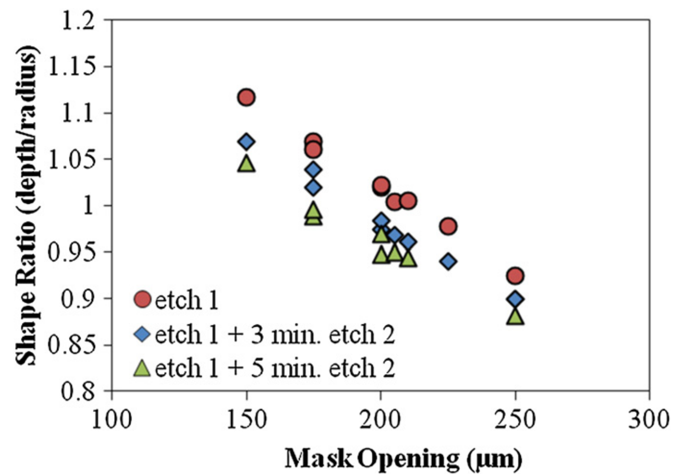

Figure 7. Shape ratio for different mask openings after successive etching steps.

The mask opening data suggests that an opening of 200–215 μm would be able to give a semi-circular cross-section with a radius of 260–280 μm, and was therefore selected as the opening for future isotropic etching experiments. It should be noted that the mask opening was chosen to err on the side of being slightly wider than a perfect circular cross section so as not to inadvertently create a raceway too narrow for the ball.

Once the mask opening was determined, the bulk of the experiment was focused on the careful manipulation of *etch 1* plasma parameters in order to finely tune the raceway geometry. As discussed earlier, the plasma properties of interest were primarily the chamber pressure and RF plate power. Eight identical wafers were prepared with arrays of test raceways patterned with photolithography in 10 μm thick *AZ9260* photoresist. Each wafer was etched for 65 min to obtain near final dimensions. The parameters of interest were vertical and lateral etch rates, roughness, curvature and photoresist selectivity. Table 3 presents the pertinent etch conditions and the resulting parameters.

Recipes 1 through 6 were etched at a constant chamber pressure with variable RF plate power. The principle difference amongst them is the curvature of the bottom of the raceway and the selectivity of etching the substrate versus masking material, which is important for designing a final fabrication process flow. Varying the RF plate power will change the strength of the magnetic field that directs the plasma ions to the surface of the substrate. In general, the ICP etching mechanism is a combination of chemical etching from the fluorination and subsequent volatilization of silicon, and physical etching from the sputtering of surface atoms by plasma ions. The range of plate powers tested (6–16 W) is not expected to produce ions with enough energy to overcome the 4.62 eV binding energy

Table 3. Parametric *Etch 1* study.

<table>
<tr><th colspan="9">Universal Parameters</th></tr>
<tr><td colspan="2">Plate power (W)</td><td>Chamber pressure (mTorr)</td><td colspan="2">RF coil power (W)</td><td colspan="2">Plate temp (°C)</td><td>SF_6 flow (sccm)</td><td>Ar flow (sccm)</td></tr>
<tr><td colspan="2">variable</td><td>variable</td><td colspan="2">850</td><td colspan="2">30</td><td>100</td><td>40</td></tr>
<tr><th colspan="3">Process</th><th colspan="6">Geometric Parameters</th></tr>
<tr><th>Recipe</th><td>Plate power (W)</td><td>Chamber pressure (mTorr)</td><td>Vertical rate (µm/min)</td><td>Lateral rate (µm/min)</td><td>Roughness (RMS µm)</td><td>Curvature (µm)</td><td colspan="2">Etch selectivity</td></tr>
<tr><td>1</td><td>6</td><td>22</td><td>3.6</td><td>2.0</td><td>>0.02</td><td>524</td><td colspan="2">95.4</td></tr>
<tr><td>2</td><td>8</td><td>22</td><td>3.7</td><td>2.1</td><td>>0.02</td><td>518</td><td colspan="2">84.8</td></tr>
<tr><td>3</td><td>10</td><td>22</td><td>3.7</td><td>2.0</td><td>>0.02</td><td>518</td><td colspan="2">75.9</td></tr>
<tr><td>4</td><td>12</td><td>22</td><td>3.8</td><td>2.0</td><td>>0.02</td><td>516</td><td colspan="2">64.2</td></tr>
<tr><td>5</td><td>14</td><td>22</td><td>3.7</td><td>1.9</td><td>>0.02</td><td>368</td><td colspan="2">41.5</td></tr>
<tr><td>6</td><td>16</td><td>22</td><td>3.7</td><td>2.0</td><td>>0.02</td><td>352</td><td colspan="2">39.9</td></tr>
<tr><td>7</td><td>12</td><td>27</td><td>4.0</td><td>2.3</td><td>0.11</td><td>532</td><td colspan="2">87.9</td></tr>
<tr><td>8</td><td>12</td><td>17</td><td>3.4</td><td>1.8</td><td>0.14</td><td>422</td><td colspan="2">35.2</td></tr>
</table>

of silicon. This implies the etch process here is significantly chemical and explains the consistent etch rates observed in the system, e.g., if higher plate powers increased the etch rate, then there would be some physical etching mechanism at play. The significant change in selectivity, however, shows that the masking material does undergo physical sputtering, and is therefore less effective at high plate powers. The reduction in curvature at higher powers can be explained by the enhanced density of ions delivered to the bottom of the trench versus the sidewalls by the increased directionality of the ion paths. It should also be noted that sample 4 served as the recipe for the mask opening relationship study and was utilized as the baseline for the parametric study.

Chamber pressure was compared amongst recipes 4, 7 and 8. The physical implications of chamber pressure are complicated because of the competing effects of plasma density and a change in the MFP of the plasma molecule. Longer MFP ions travel further without a collision at lower pressures versus higher pressures, implying that the ions will have slightly more time to accelerate and will therefore hit the surface with a higher energy. Higher pressures may reduce the MFP, but increase the plasma density and therefore the number of reactive species on the surface. Based on the etch rates from table 3, the increased plasma density accelerated etching. The diameter of curvature obtained ranged from 422 to 532 μm as pressure was raised from 17 to 27 mTorr, which is expected based on the reduced directionality of ions in higher-pressure plasmas. The surface roughness was significantly affected by the change in chamber pressure, with both high (27 mTorr) and low (17 mTorr) pressures significantly increasing the surface roughness. At high pressures, ion bombardment energy is reduced due to the shortened MFP; therefore, the roughness will be dictated by enhanced chemical etching. At low pressures, ion bombardment energy is higher; therefore, the surface roughness is likely due to enhanced physical etching. Minimum roughness is obtained when the chemical and physical etches are tuned properly. A

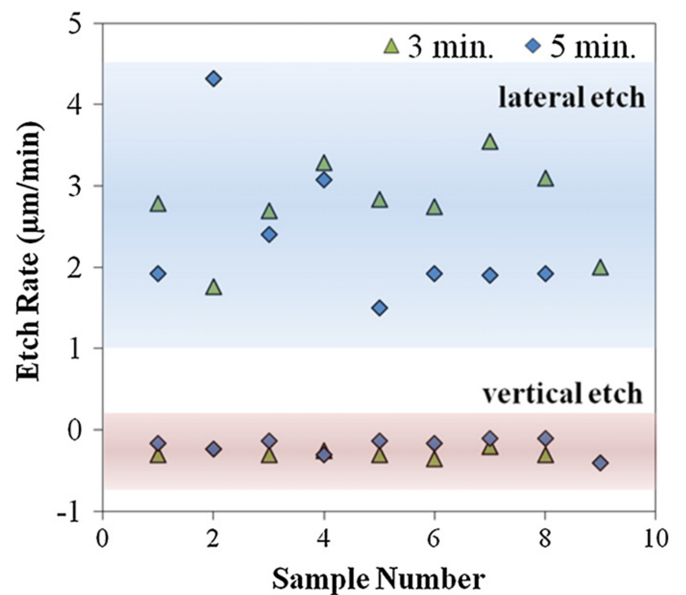

Figure 8. A comparison of etch rates for vertically and laterally for the blanket etch step after 3 and 5 min of etching. The negative vertical etch rate is a result of the thinning of the wafer.

similar relationship with chamber pressure and roughness was observed by Chen in his thesis work on ICP etching [25].

Etch 2 was a blanket etch, using the parameters from recipe 4, taking place after the masking material was removed post-*etch 1*. *Etch 2* was used to target the re-entrant edges left after *etch 1* (see figure 6), which are etched away due to being exposed on both sides and being thin compared to the surface of the wafer and the semi-circular raceway. A comparison of the etch rates of two blanket etches is presented below in figure 8.

The lateral etch rate ranges from 1.9 to 4.3 μm min^{-1}, which is a function of the sharpness of the initial re-entrant profile. The vertical etch rate was slightly negative relative to the top surface of the wafer, a function of broad wafer thinning.

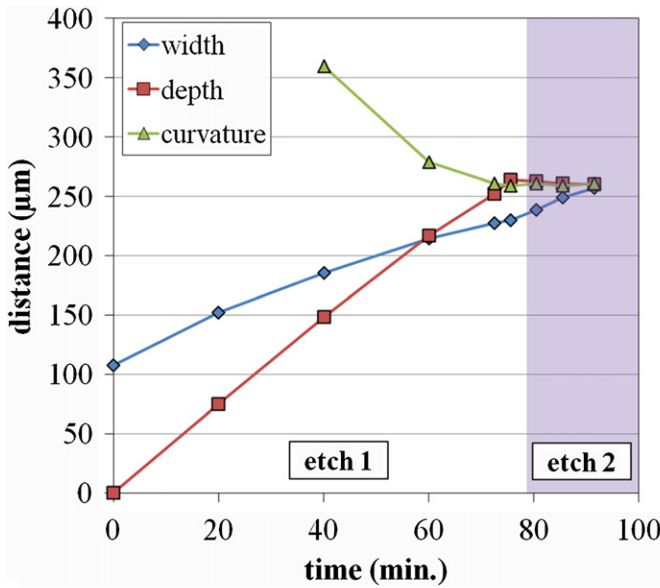

Figure 9. Evolution of raceway geometry through multi-step etching process.

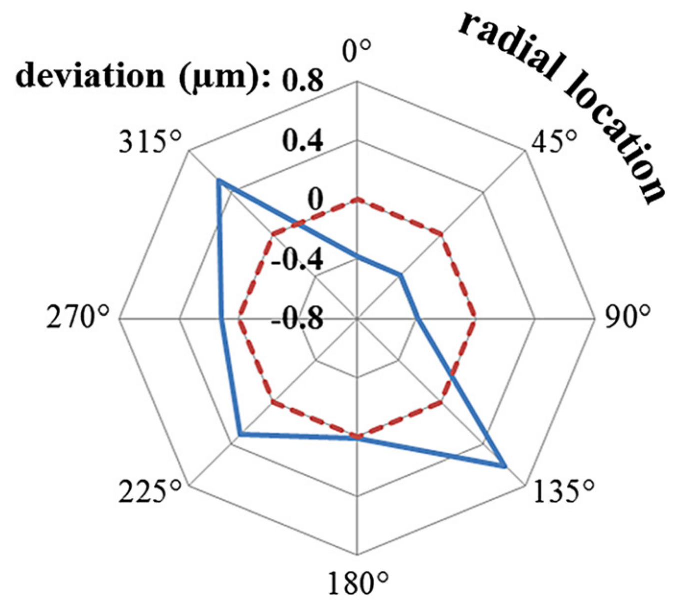

Figure 10. Radial plot of raceway depth variation. The average depth is plotted at '0' and deviation is either positive (deeper than average) or negative (shallower than average).

The power and pressure parameters of *etch 2* were not found to have a significant impact on the etch geometry and were therefore not optimized.

Finally, the two-step etching process was integrated into the microfabrication flow of the microturbine, described in the previous section. The final mask opening was selected to be 215 μm, recipe 2 was selected for *etch 1* and recipe 4 was utilized for the blanket *etch 2*. The raceway etching was performed in 2 to 20 min intervals to better understand the evolution of the raceway geometry. The depth, width and curvature radii of the final raceway etch are presented in figure 9.

The bulk of the material is removed during the *etch 1* step and the curvature and depth nearly reach their final values. The curvature of the raceway would ideally represent the entire raceway, but for this work it is a measurement of the curvature at the bottom of the raceway, as shown in figure 6. Since the ball will only make contact with an area on the bottom of the raceway, the curvature of the whole raceway is not critical, as long as it does not reduce the diameter of the raceway to the point where it impedes the motion of the ball. When the depth, width and curvature all converge on a single value, as shown in figure 9, then it can be assumed the raceway is nearly a perfect semi-circle, which is confirmed in cross-section SEM images of the device shown in the section 4.2. It is also interesting to note that there is some nonlinearity in the lateral rate, with the etching slowing down towards the end of *etch 1*. This is a result of a minor starvation of reactants to the undercut sidewalls. The final raceway uniformity was measured by optical profilometry and presented in figure 10. It is important to minimize variation in raceway depth to minimize out-of-plane vibration in the rotor during operation which can lead to premature device failure.

An average variation of 340 nm, or 0.15% of the raceway depth around a 5 mm diameter rotor was measured. This value of uniformity is on par with well-tuned DRIE and very good for isotropic etching techniques [26].

Upon completion of the raceway etch, the wafer was spray-coated with *AZ 4999* photoresist to cover the inside surfaces of the raceway to mask the offset release etches. The offset release pattern lithography was compensated to take into account the curved substrate and UV light spreading. SEM images of a completed raceway with the offset release etch as well as a bonded microturbine with the turbine impeller structure removed is shown below in figure 11.

4.2. Microturbine performance

Three variations of the deep-grooved raceway microturbine were tested, employing two rotor diameters (2.5 and 5 mm) and two ball materials (steel and silicon carbide). The first set of tests was performed on raceways that were 512 μm in diameter, providing 12 μm of clearance for these devices. Testing is performed by monitoring the turbine operating parameters: flow, pressure and speed, through an acrylic package (figure 5). A custom LABVIEW^{TM} interface was created to control the device and acquire data.

The 5 mm rotor with SiC balls variation was the first device tested. It was operated successfully above 65 krpm before catastrophic failure (shown in figure 12). The normal load on the rotor was 30 mN at 65 krpm, which resulted in a contact angle between 25° and 40°, allowing the ball to make contact with the offset release etch. It is assumed that the raceway facture was initiated at the sharp contact point where the offset etch meets the raceway. Once fracture was initiated on the raceway, the rotor became unstable and completely fractured the raceway over a time period of $<$10 s. Testing of this turbine was an experimental confirmation of the limits set forth from the numerical simulation.

A drop below the 37° contact angle minimum is observed just before bearing failure. The erratic nature of

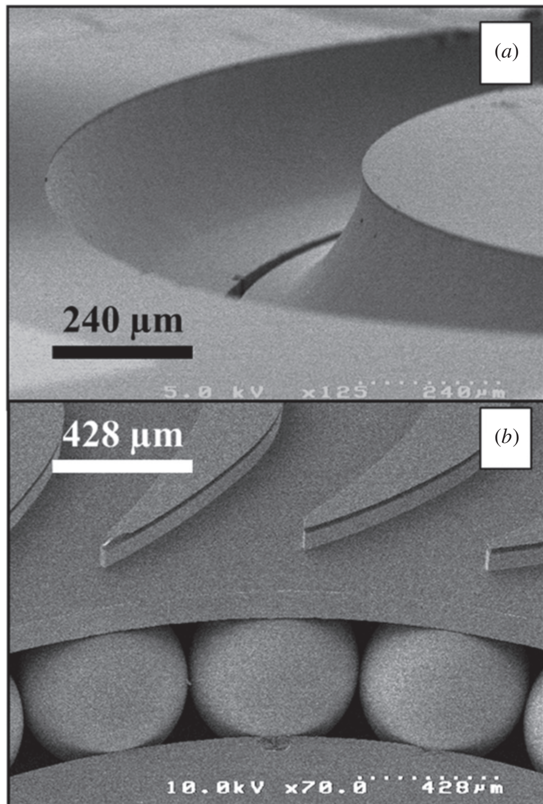

Figure 11. SEM images of microturbine. (*a*) Completed raceway with nested offset release etch visible. (*b*) Bonded device with turbine impeller removed.

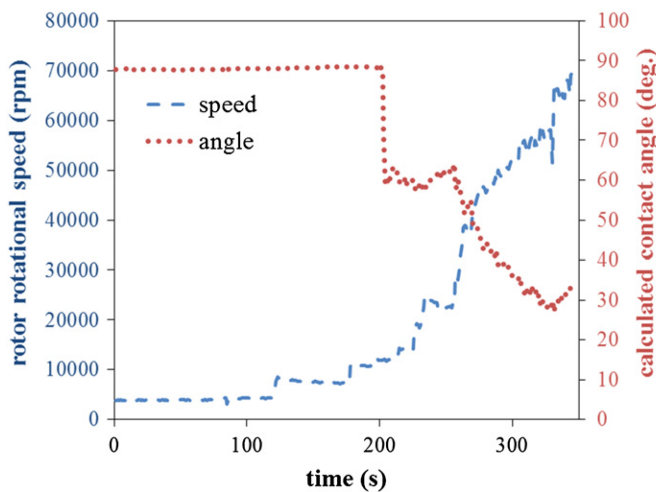

Figure 12. Operation of the first isotropic bearing-containing microturbine, showing measured rotor speed and calculated contact angle.

the contact angle comes from human error in the operation of the device. Actuation flow and thrust flow are controlled manually, therefore adjustments are made discretely and there is lag between adjustments and microturbine response. Future systems could integrate a contact angle calculator and adjust flows to maintain a desired contact angle for a given speed.

The next turbine tested was the 2.5 mm diameter, silicon carbide ball containing device. The rotor was actuated to

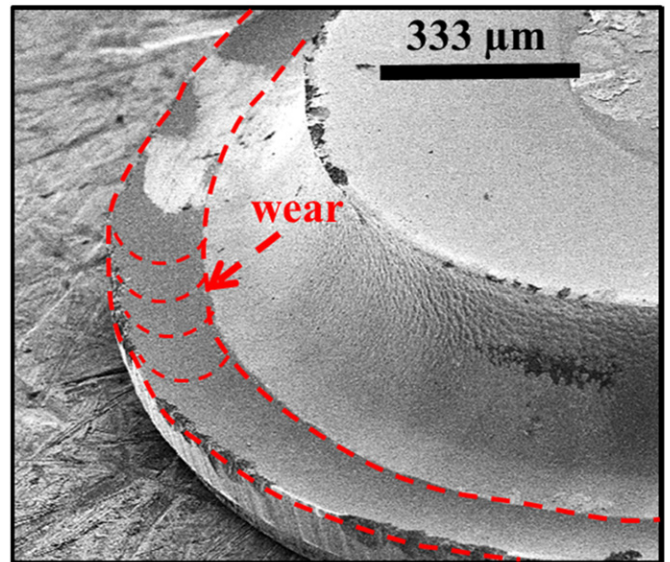

Figure 13. SEM of worn raceway from 2.5 mm rotor with silicon carbide balls. Wear area is highlighted.

47 krpm under 15 mN rotor normal load, resulting in a calculated contact angle of 47°, over the geometrically defined 37° limit. This device was actuated for 5 min and then disassembled to observe the wear using SEM (figure 13).

The wear observed in figure 13 was of an abrasive nature, with the harder SiC balls removing material from the Si raceways. The effect was significant, measuring 1–2 μm of removed raceway material within the contact area of both the top and bottom ellipsis. This abrasive wear is due to the significant sliding motion imparted by the geometry of the raceway, discussed in section 2.1. Higher normal loads would reduce the magnitude of the sliding by shifting the contact ellipse towards perpendicular of the axis of rotation of the ball and allow for better rolling. Lubrication has also been shown to work well in the case of sliding-regime wear [27], and is the subject of future studies.

A second set of microturbines were fabricated with much larger tolerances in order to reduce the size of the contact ellipse, thereby reducing the amount of sliding in the system. The tested microturbine was 2.5 mm in diameter and contained stainless-steel balls. The diameter of the raceway was measured to be 560 μm, resulting in 60 μm of side-to-side play. This width was chosen to give ample room for the ball during encapsulation and bonding, as well as a 38% decrease in contact area at 100 mN rotor normal load for the 2.5 mm SS device. The testing of the device is shown in figure 14.

The device begins spinning at 40 krpm, then quickly fails. This pattern of on/off operation continues with a general trend towards decreasing operating speeds. As a point of reference, it requires 11 W of input power to operate this microturbine at 10 krpm compared to 0.05 W to operate the microturbine described in [18]. The bearing and turbine inefficiencies are convoluted in the input power versus speed comparison; therefore it is difficult to determine the source of the performance difference. From the turbine efficiency standpoint, the device with the isotropic bearings has 100 μm tall blades and 60 μm of rotor sag, leaving 40 μm of exposed

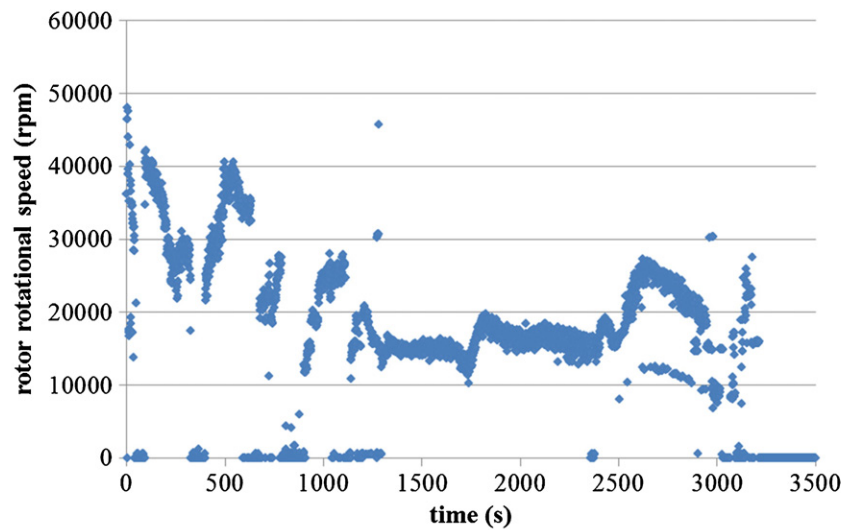

Figure 14. Operation of a 2.5 mm SS microturbine with isotropic raceways.

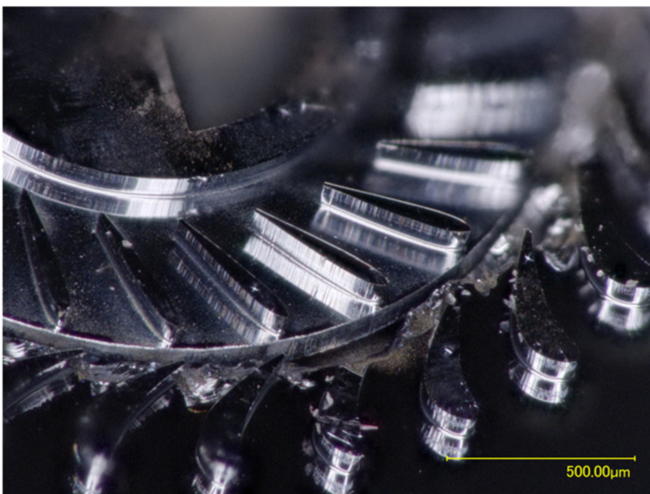

Figure 15. Photograph of 2.5 mm rotor diameter, stainless-steel ball device after testing.

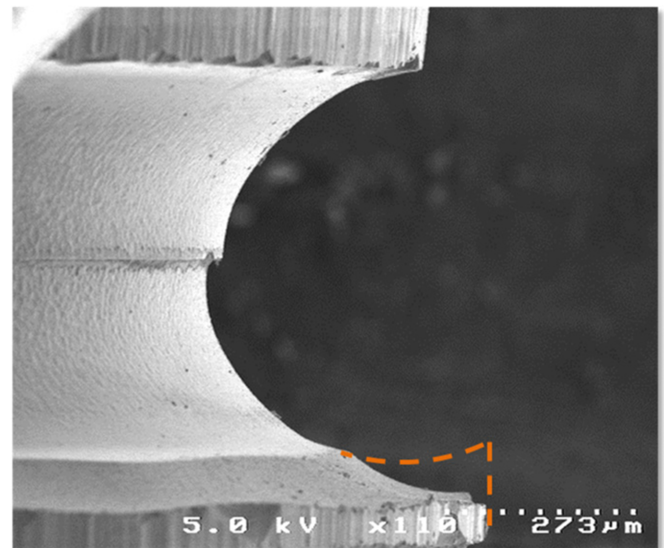

Figure 16. SEM of 2.5 mm, stainless-steel device after 3000 s of operation. An estimate of the original raceway profile is shown.

turbine structure, compared to 250 μm tall blades with 10 μm of sag for the microturbine described in [18]. Therefore it is estimated that the difference in performance has a significant turbine efficiency component.

The second major influence on the device performance is the side-to-side play allowed for in the rotor. The deep-groove devices used 560 μm diameter raceways for 500 μm balls and 20 μm journal bearings defined by the offset release etch, meaning the rotor and stator are allowed to come into direct contact without obstruction from the ball. An image of the tested devices is shown in figure 15.

Significant wear, in the form of brittle fracture, can be observed on the stator around the journal release etch. This is due to the side-to-side play in the device during operation allowed for by geometry. The stop/start behavior of the device was likely caused by the generation and removal of fractured stator material.

SEM inspection of the raceway after 3000 s of discontinuous operation revealed a significant amount of abrasive wear. The abrasive wear mechanism, caused by sliding, was observed in figure 13 for the silicon carbide balls after 300 s, and is shown for the 2.5 mm stainless-steel ball device in figure 16.

During operation, the ball wore away a second radius within the grooved raceway. The original raceway profile is shown by the orange dashed line, estimated from known geometries. It should also be noted that there is some slight bond misalignment observed for this device ($<$20 μm), which will affect the device performance by introducing side-to-side motion. The significant amount of abrasive wear comes from the sliding discussed in section 2.1, which is inherent in the deep-groove design. Future devices should utilize lubrication

or new geometries to limit solid–solid contact, or reduce the magnitude of sliding.

Three devices utilizing deep-groove raceway geometry were fabricated and tested, comparing the effects of different geometries and ball materials, while testing the new raceway geometry. Challenges arose with the operation, wear and geometry of the devices, so the ultimate goal of high-speed, reliable operation was not realized, but speeds in excess of 65 krpm were obtained briefly. Next generation microturbines utilizing deep-groove geometry should utilize taller turbine structures, wider journal bearings, and lubrication for improved device performance.

5. Conclusions

This work presents the development of a 3D fabrication technique with the potential of significantly improving the performance of micro-scale rotary structures. The utilization of microball bearings for MEMS has shown great promise through an array of demonstrations, but there has always been a fundamental speed limit set by geometries limited by fabrication techniques. By developing a process to create uniform, smooth and curved surfaces, micro-scale ball-bearings are then able to be utilized in regimes where load can be accommodated for both axially and radially. Accordingly, a dynamic model of the bearing system was developed around the obtainable microfabricated geometry.

A two-step etching process for deep-groove bearing raceways was developed around the specific goal of integration within a microturbine testing structure. The first etch step was parametrically studied to optimize depth, width and curvature, while maintaining good raceway uniformity and low roughness. The second etch step was performed to remove the re-entrant etch profile, widening the raceway. Single device non-uniformity in raceway depth was measured to be $<0.15\%$.

Three different microturbines were fabricated to act as the test platform for the new raceway geometries. While it allowed for devices to be operated stably up to 70 krpm, the device suffered from significant sliding friction created by the sloping raceways. It was also found that it is critical to maintain the proper ratio of axial to radial load so the angle of contact is maintained within the designed geometric constraints, or catastrophic failure is probable.

Future work will utilize the 3D fabrication technique first described in this paper to create a true angular contact bearing. This will reduce the sliding friction in the system and potentially increase device lifetimes, at the expense of fabrication complexity. Micro-scale lubrication schemes compatible with the microturbine platform will also be explored as a second route to mitigating sliding friction.

Acknowledgments

This work was supported by the US National Science Foundation under award no. 0901411. The authors would like to acknowledge Mr Saswat Misra and Mr Jeremy Feldman for their assistance in the experiment. The authors would also like to acknowledge the U.S. Army Research Laboratory Cleanroom Staff.

References

[1] McCarthy M, Waits C M, Beyaz M I and Ghodssi R 2009 A rotary microactuator supported on encapsulated microball bearings using an electro-pneumatic thrust balance *J. Micromech. Microeng.* **19** 094007

[2] McCarthy M, Waits C M and Ghodssi R 2009 Dynamic friction and wear in a planar-contact encapsulated microball bearing using an integrated microturbine *J. Microelectromech. Syst.* **18** 263–73

[3] Waits C M, McCarthy M and Ghodssi R 2010 A microfabricated spiral-groove turbopump supported on microball bearings *J. Microelectromech. Syst.* **19** 99–109

[4] Beyaz M, Hanrahan B, Feldman J and Ghodssi R 2012 An integrated micro-turbo-generator supported on encapsulated microball bearings *Int. Conf. on Micro Electro Mechanical Systems (Paris, France)* pp 1209–12

[5] Ghodssi R, Hanrahan B and Beyaz M 2011 Microball bearing technology for MEMS devices and integrated microsystems *Transducers'11: 16th Int. Conf. on Solid-State Sensors, Actuators, and Microsystems (Beijing, China)* pp 1789–94

[6] Waits C M, Morgan B, Kastantin M and Ghodssi R 2005 Microfabrication of 3D silicon MEMS structures using gray-scale lithography and deep reactive ion etching *Sensors Actuators* a **119** 245–53

[7] Morgan B, McGee J and Ghodssi R 2007 Automated two-axes optical fiber alignment using grayscale technology *J. Microelectromech. Syst.* **16** 102–10

[8] Bertsch A, Lorenz H and Renaud P 1999 3D microfabrication by combining microstereolithography and thick resist UV lithography *Sensors Actuators* A **73** 14–23

[9] Bichler S *et al* 2012 Functional flexible organic-inorganic hybrid polymer for two photon patterning of optical waveguides *Opt. Mater.* **34** 772–80

[10] Madden J D and Hunter I W 1996 Three-dimensional microfabrication by localized electrochemical deposition *J. Microelectromech. Syst.* **5** 24–32

[11] Tseng A A 2004 Recent developments in micromilling using focused ion beam technology *J. Micromech. Microeng.* **14** R15–34

[12] Robbins H and Schwartz B 1960 Chemical etching of silicon: 2. The system HF, HNO_3, H_2O, and $HC_2H_3O_2$ *J. Electrochem. Soc.* **107** 108–11

[13] Schwartz B and Robbins H 1976 Chemical etching of silicon: 4. Etching technology *J. Electrochem. Soc.* **123** 1903–9

[14] Marcos G, Rhallabi A and Ranson P 2003 Monte Carlo simulation method for etching of deep trenches in Si by a SF_6/O_2 plasma mixture *J. Vac. Sci. Technol.* A **21** 87–95

[15] Azimi S, Sandoughsaz A, Amirsolaimani B, Naghsh-Nilchi J and Mohajerzadeh S 2011 Three-dimensional etching of silicon substrates using a modified deep reactive ion etching technique *J. Micromech. Microeng.* **21** 074005

[16] Gantz K, Renaghan L and Agah M 2008 Development of a comprehensive model for RIE-lag-based three-dimensional microchannel fabrication *J. Micromech. Microeng.* **18** 025003

[17] Larsen K P, Ravnkilde J T and Hansen O 2005 Investigations of the isotropic etch of an ICP source for silicon microlens mold fabrication *J. Micromech. Microeng.* **15** 873–82

[18] Hanrahan B, Beyaz M, McCarthy M, Waits C and Ghodssi R 2010 A new performance regime for microfabricated ball bearings *MEMS'10: Proc. of Power (Leuven, Belgium)* pp 191–4

[19] Hanrahan B, Feldman J, Misra S, Mitcheson P D, Waits C and Ghodssi R 2012 Off-the-shelf MEMS for rotary MEMS

Int. Conf. on Micro Electro Mechanical Systems (Paris, France) pp 579–82

[20] Waits C M, Geil B and Ghodssi R 2007 Encapsulated ball bearings for rotary micro machines *J. Micromech. Microeng.* **17** S224–9

[21] Hertz H 1896 *Miscellaneous Papers* (London: Macmillan) pp 146–62

[22] Hanrahan B 2013 Tribology of microball bearing MEMS *Doctor of Philosophy, Materials Science and Engineering* University of Maryland

[23] Knizikevicius R 2010 Simulations of Si and SiO(2) etching in SF(6)+O(2) plasma *Acta Phys. Pol.* A **117** 478–83

[24] Larsen K P, Petersen D H and Hansen O 2006 Study of the roughness in a photoresist masked, isotropic, SF_6-based ICP silicon etch *J. Electrochem. Soc.* **153** G1051–8

[25] Chen H 2000 Inductively coupled plasma etching of InP *Masters of Science, Metallurgy and Materials Science* (Toronto: University of Toronto)

[26] Hill T 2004 Analysis of DRIE uniformity for microelectromechanical systems *Masters of Science, Electrical and Computer Science* (Cambridge, MA: Massachusetts Institute of Technology)

[27] Asay D B, Dugger M T, Ohlhausen J A and Kim S H 2007 Macro- to Nanoscale wear prevention via molecular adsorption *Langmuir* **24** 155–9